Smaller is Softer

Benzerga, A.A.; Hong, S.S.; Kim, K.S.; Needleman, A.; van der Giessen, E.

Published in:
Acta Materialia

DOI:
10.1016/S1359-6454(01)00195-1

Publication date:
2001

Pergamon

Acta mater. 49 (2001) 3071–3083

Acta MATERIALIA

www.elsevier.com/locate/actamat

SMALLER IS SOFTER: AN INVERSE SIZE EFFECT IN A CAST ALUMINUM ALLOY

A. A. BENZERGA[1], S. S. HONG[1], K. S. KIM[1], A. NEEDLEMAN[1]† and E. VAN DER GIESSEN[2]

[1]Brown University, Division of Engineering, Providence, RI 02912, USA and [2]University of Groningen, Department of Applied Physics, Nijenborgh 4, 9747 AG Groningen, The Netherlands

(Received 2 March 2001; received in revised form 30 April 2001; accepted 30 April 2001)

Abstract—The stress–strain curves of A356 cast aluminum alloys exhibit an unusual size effect on flow properties: the finer the microstructure, the lower the tensile flow strength. Tensile tests were carried out on specimens made of an A356 alloy with 7% Si as the main alloying element. The specimens were cast at two cooling rates. For both processing conditions the microstructure within each grain consists of pro-eutectic aluminum dendrites separated by a boundary eutectic region of segregated silicon particles of ≈2–3 μm diameter. The fast cooling rate gives rise to a secondary dendrite arm spacing of approximately 20–30 μm, while the secondary dendrite arm spacing obtained with the slow cooling rate is about 80–100 μm. Discrete dislocation plasticity is used to model the inverse size effect in this alloy. The dislocations are represented as line defects in an elastic solid and dislocation nucleation, annihilation and drag are incorporated through a set of constitutive rules. Obstacles to dislocation motion are randomly distributed in the dendrite and the eutectic regions, but with different densities and strengths. The thickness of the eutectic region is found to be a key parameter in determining the inverse size effect. In addition, the size effect is found to depend on the extent to which dislocation nucleation takes place in the eutectic region.

Keywords: Microstructure; Plasticity; Dislocations; Aluminum alloys

1. INTRODUCTION

There is clear experimental evidence that plastic flow processes in crystalline solids are inherently size dependent over a scale that ranges from a fraction of a micron to a hundred microns or so, e.g. [1–8], with smaller being harder. One source of this size dependence is that internal obstacles, such as incoherent precipitates and grain and phase boundaries, restrict glide, leading to dislocation pile-ups which further restrict dislocation motion. As a consequence, the strength increases as the scale of the microstructure decreases, as noted first by Hall [1] and Petch [2]. Geometrically necessary dislocations, Nye [3] and Ashby [4], which can arise from restricted slip induced strain gradients, also lead to increased strength at smaller sizes. On the other hand, at very small size scales, say on the order of tens of nanometers, smaller is not necessarily harder. For example, in nanocrystalline materials, the Hall–Petch effect can be either absent or reversed [9, 10], as a result of grain boundary sliding.

Here, we report on tensile tests carried out on specimens made of an A356 cast aluminum alloy with 7% Si as the main alloying element, cast at two cooling rates. For both processing conditions the microstructure within each grain consists of pro-eutectic aluminum dendrites separated by a boundary eutectic region of segregated silicon particles. The fast cooling rate gives a significantly finer microstructure than the slow cooling rate. The size of the pro-eutectic dendrites and the boundary eutectic region scale together, with the average spacing between pro-eutectic dendrites being the secondary dendrite arm spacing (of the order of tens of microns). In contrast to expectations at this scale, the fine microstructure exhibits a softer plastic response than the coarse microstructure.

In order to explore the mechanism for this inverse size effect, calculations are carried out using a simple discrete dislocation model. The model consists of a planar doubly periodic array of cells, each of which consists of matrix material representing the pro-eutectic aluminum dendrites and wall material representing the silicon particle rich boundary eutectic region. The array is subject to remote simple shear. Single slip by

† To whom all correspondence should be addressed. Tel.: +1-401-863-2863; fax: +1-401-863-1157.

E-mail address: needle@engin.brown.edu (A. Needleman)

1359-6454/01/$20.00
PII: S1359-6454(01)00195-1

the motion of edge dislocations is assumed on slip planes parallel to the shear direction and normal to the wall. Drag during dislocation motion, interactions with obstacles, and dislocation nucleation and annihilation are also accounted for. The boundary value problem formulation and solution procedure follow that used in Ref. 11 to analyze composite response, although here the material has uniform elastic properties.

The wall material differs from the matrix material in the density and strength of dislocation obstacles and in the density of nucleation sources. Calculations are carried out for a range of microstructural size scales in order to explore the size dependence of the stress–strain response for several characterizations of the wall material.

Together the experiments and calculations suggest that the inverse size effect is the result of reduced effectiveness of the silicon particle rich eutectic region in blocking slip as its size decreases. If slip is not effectively blocked, smaller is not necessarily harder.

2. EXPERIMENTAL OBSERVATIONS

A set of specimens of cast aluminum alloy A356-T6 was received from the Ford Motor Company Scientific Research Laboratory. The A356 cast aluminum is close to an Al/Si binary alloy with a nominal composition of 7% Si, 0.3% Mg, 0.18% Fe, 0.15% Ti, 0.07% Zn, 0.05% Mn and 0.05% Cu. It was cast in a wedge-shaped mold with a copper chill on the thin side of the wedge [12]. Metallographic examination of the sub-grain microstructures showed those of a typical hypo-eutectic alloy system, composed of pro-eutectic aluminum dendrites surrounded by eutectic walls. The rapid cooling rate at the chilling side produced fine sub-grain microstructures of approximately 20–30 μm secondary dendrite arm spacing. The secondary dendrite arm spacing varied gradually to about 80–100 μm at the slow-cooling end of the mold. The cast specimen was then processed with hot isostatic pressure to make a pore-free sample, and was heat treated under T6 conditions.

A standard ASTM-E8 tensile test was carried out to investigate the effects of the microstructures on tensile properties of the cast aluminum. Sheet-type tensile specimens of 3 mm by 6 mm cross section and 30 mm gauge length were machined out of the two regions of fine and coarse microstructures in a single batch of the cast sample. The specimens were tested with an Instron 5051 tensile testing machine under a strain rate of 10^{-3}/s. Figure 1 shows a comparison between typical tensile stress–strain curves of specimens with the fine and coarse microstructures. Quite surprisingly, the specimen with the finer microstructure has a lower flow strength than the coarser microstructure specimen. The spread of the flow strength data for specimens of each microstructure was less than 10% of the difference between the two flow strengths. On the other hand, the scatter in the elongation data of the fine-microstructure specimens was very large — from 4% to 8% strain. Figure 1(b) shows that the main size effect is the increased hardening rate of the coarse microstructure at very small strains. A plot of the hardening modulus versus strain (not shown) reveals that although the hardening rate of the coarse microstructure is initially greater than that of the fine microstructure, at larger strains the two hardening rates essentially coincide.

A similar trend in flow strength variation was observed by McLellan [13] in the aluminum alloy A357-T6, which has a slightly higher Mg content than that in A356-T6, for a range of secondary dendrite arm spacings between 55 and 70 μm. However, the size anomaly was not so clear because the size range over which it occurred was narrow and the magnitude of the effect was not as large as for A356-T6 because of the relatively higher flow strength of the A357 alloy, so that the percentage increase in flow strength was smaller than seen here. Indeed, the magnitude of the flow strength reversal in Ref. 13 was comparable to the statistical non-uniformity of the sample properties.

A set of microscopic studies showed that the silicon particles in the eutectic wall region have a diameter of approximately 2–3 μm. As the eutectic wall region is a composite of silicon particles in an aluminum matrix, the nominal hardness in this region is higher than that of the pro-eutectic aluminum region. The nominal micro-hardness of the eutectic wall region was measured with a Vickers micro-hardness tester. A 10 g load was applied to make the micro-hardness indentation size "D" of 10 to 15 μm in the diagonal directions. The results of the test are shown in Fig. 2. The hardness varies near the boundary between the eutectic wall ($X<0$) and the pro-eutectic aluminum ($X>0$) regions, as shown in the figure. The hardness is approximately 0.89 GPa and 0.77 GPa in the eutectic wall and in the pro-eutectic aluminum regions, respectively.

Plastic deformation at the microstructural level was observed by both optical and AFM (Atomic Force Microscope) microscopy. Figure 3(a) shows an optical micrograph of dislocation slip bands in a region of the fine microstructure material. The dislocation slip bands penetrate through the relatively thin eutectic walls of the fine microstructure. However, the slip bands do not penetrate or tunnel through the thick eutectic walls of the coarse microstructure material shown in Fig. 3(b). Since the microstructure in Fig. 3 is within a grain, initially, the slip system directions do not change across the pro-eutectic dendrite regions. In order to investigate the slip activity near the eutectic walls, the surface of a deformed specimen was scanned by an AFM (Park Scientific Instrument—Autoprobe CP) with a scan range of 80×80 μm^2 and a scan rate of three lines per second. Figure 3(c) shows the AFM surface topography of the deformed sample with the coarse microstructure. The

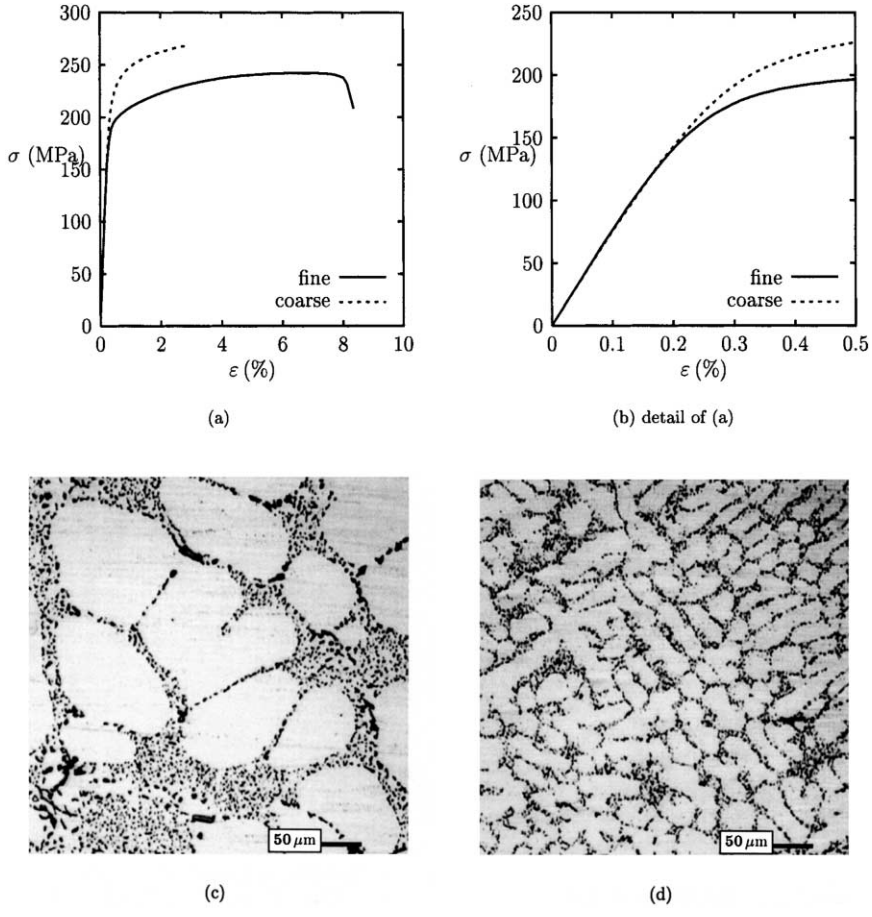

Fig. 1. (a) and (b) Effect of the sub-grain microstructure on the overall response of cast aluminum A356 in uniaxial tension. The secondary dendrite arm spacing is about 80–100 μm, micrograph (c), and 20–30 μm, micrograph (d).

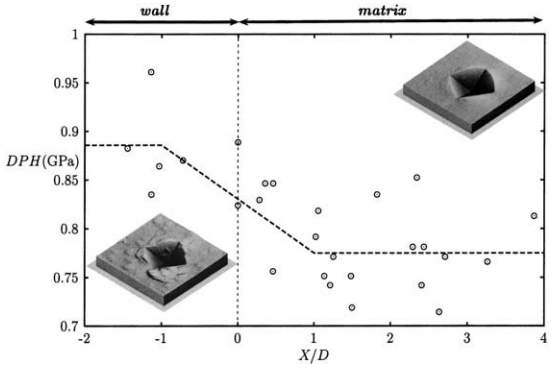

Fig. 2. Distribution of Vickers micro-hardness DPH near the interface between wall and matrix. D is the indentation size in the diagonal directions.

surface steps observed in this topography are caused by the screw components of dislocations swept across the surface. Unlike conventional dislocation observation techniques, such as the method of etch pits or transmission electron microscopy, the AFM surface topography provides the slip trajectory of dislocations rather than current positions of the dislocations. As seen in this figure, the surface step height mostly reduces as it approaches the eutectic wall. This indicates that the dislocations were mostly nucleated in the pro-eutectic aluminum region and piled up at the wall boundary. Some of the traces indicate that the dislocation slip bands have penetrated or tunneled through the thin wall region.

3. MODEL FORMULATION

The cast aluminum alloy is modeled as containing two "phases" with the same elastic properties but different plastic properties. The two phases are referred to as the matrix material (the pro-eutectic aluminum dendrites) and the wall material (the eutectic boundary region), respectively. A doubly periodic stacking of elementary cells subject to simple shear is analyzed, with a unit cell as depicted in Fig. 4. A reference unit cell of width $2\times L$ and height L is used which contains wall material of width $W = fL$, with f being the area fraction of the boundary eutectic region.

A plane strain analysis is carried out with shear imposed by prescribing displacement rates on the top and bottom of the unit cell,

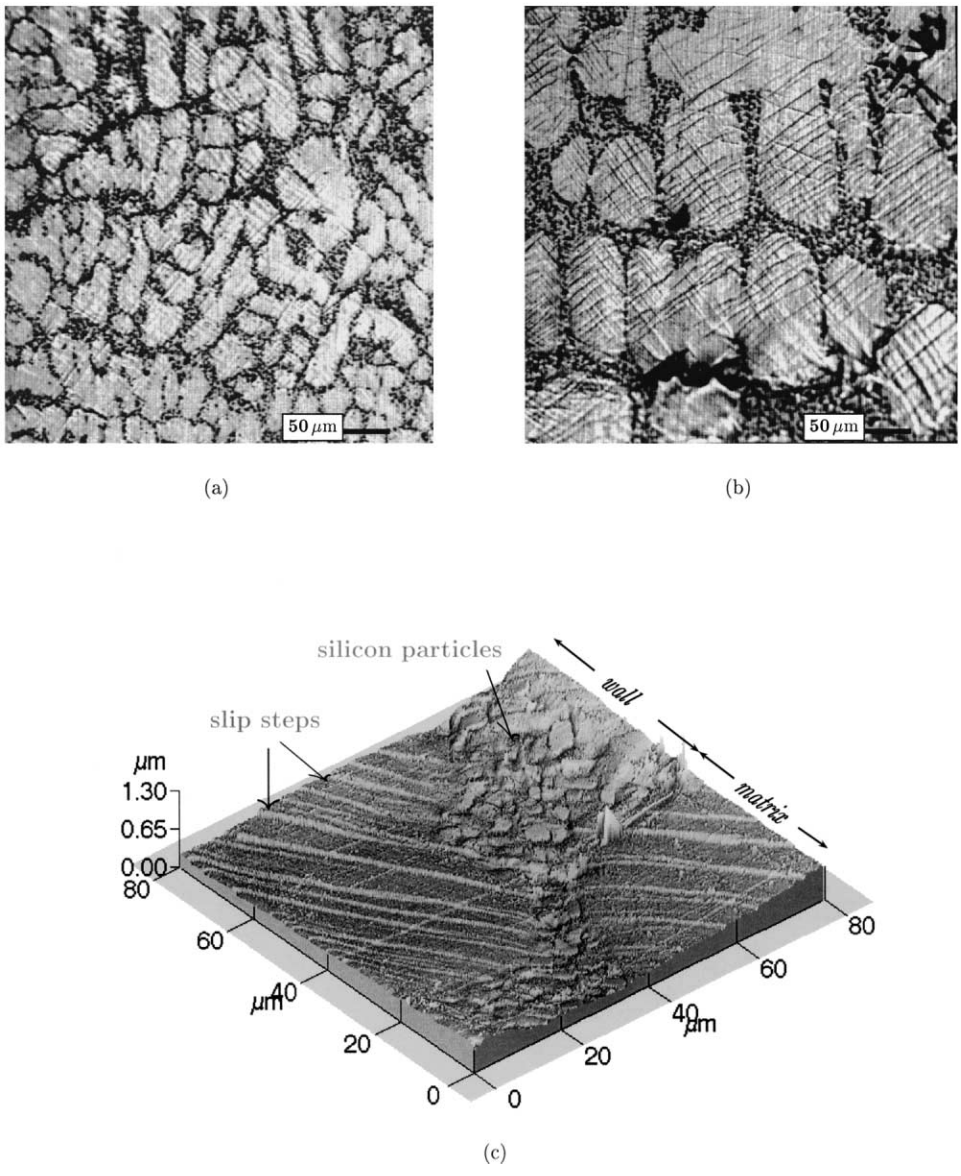

Fig. 3. Observation in light microscopy of deformed samples with coarse (a) and fine (b) microstructures. (c) AFM topography showing pile-up of dislocations near the matrix–wall interface.

$$u_1(x_1,\pm L/2;t) = \pm Vt \quad u_2(x_1,\pm L/2;t) = 0, \qquad (1)$$

where V is the applied velocity. Periodic boundary conditions are imposed along the lateral sides $x_1 = \pm L$. Only one slip system is considered, with the slip plane normal **n** being in the x_2-direction so that the glide direction **m** and the shearing direction coincide. All dislocations are of edge character and have the same magnitude b of the Burgers vector.

The dislocations are modeled as line defects in a linear elastic, isotropic solid. Thus, the long-range interactions between dislocations are accounted for through the continuum elasticity fields. The short-range interactions are incorporated into the formulation through a set of constitutive rules which are based on those proposed by Kubin *et al*. [14]. In this formulation, both the plastic stress–strain response and the evolution of the dislocation structure are outcomes of the boundary value problem solution. Details of the boundary value problem formulation and solution are given in Ref. 11 along with additional references. The procedure is briefly outlined here.

The material is initially dislocation free. Frank–Read sources are simulated to generate new dislocations. In two dimensions, the dislocation loop emitted by such a source is modeled as a dipole. Nucleation is taken to occur at a critical value, $b\tau_s$, of the Peach–Koehler force at the source location. An

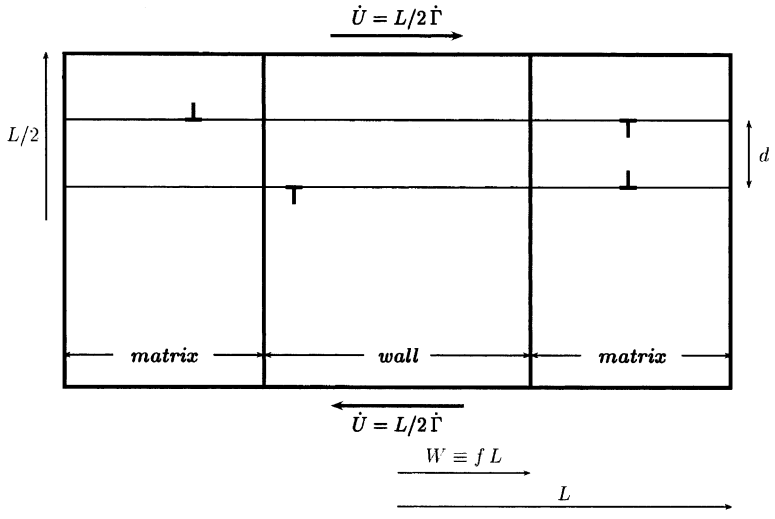

Fig. 4. Reference unit cell of the idealized two-phase material under simple shear. Periodicity is assumed and the slip planes are parallel to the shear direction.

additional nucleation parameter is the time it takes to generate the dislocation loop, t_{nuc}. The size of the generated dipole is taken according to

$$L_{\text{nuc}} = \frac{\mu}{2\pi(1-\nu)}\frac{b}{\tau_{\text{nuc}}}, \tag{2}$$

where μ is the shear modulus and ν is Poisson's ratio. At this distance, the shear stress of one dislocation acting on the other is balanced by the resolved shear stress on the current slip plane. The strength of the dislocation sources is randomly chosen from a Gaussian distribution with mean strength $\bar{\tau}_{\text{nuc}}$.

Once nucleated, each dislocation creates a stress field which decays in magnitude with the distance from it [15, 16]. Image fields due to the actual boundary conditions are incorporated through a finite element solution [17, 18]. Dislocations are restricted to move on their initial slip plane and the glide velocity $v^{(i)}$ of dislocation i is given by

$$v^{(i)} = \frac{f^{(i)}}{B} \tag{3}$$

where B is the drag coefficient and $f^{(i)}$ is the Peach–Koehler force. Because of the periodicity, when the dislocations move, they may leave the cell at $x_1 = \pm L$ but then they re-enter at the opposite side $x_1 = \mp L$. Annihilation of two dislocations with opposite Burgers vector occurs when they are sufficiently close together. This is modeled by eliminating two dislocations when they are within a material dependent, critical annihilation distance L_e.

Obstacles to dislocation motion are modeled as fixed points on a slip plane. Pinned dislocations can only pass the obstacles when their Peach–Koehler force exceeds an obstacle dependent value, $b\tau_{\text{obs}}$. In the matrix, such obstacles model the effects of forest dislocations or small precipitates, while, in addition, in the wall material they also represent the segregated silicon particles. Obstacles are randomly distributed in both regions but their density and strength distributions are independently assigned in each region. To account for the effectiveness of the silicon particles in blocking slip, the obstacles in the wall material are assigned a higher strength than those in the matrix. Although the obstacles provide a way of incorporating interactions with forest dislocations in a two-dimensional framework, the increasing obstacle density with deformation is not accounted for so that the actual strain hardening is somewhat underestimated.

4. RESULTS

The computations use material parameters that are representative of aluminum: $\nu = 0.3$ and $\mu = 26$ GPa, and $b = 2.5\times10^{-10}$ m. All other parameters are scaled relative to μ or b. The parameters that remain fixed are: the drag coefficient $B\dot{\Gamma} = 0.38\times10^{-11}\,\mu$ (see Ref. 14) with $\dot{\Gamma} = 10^3$ s^{-1}; the nucleation parameters: $\bar{\tau}_{\text{nuc}} = 2.3\times10^{-3}\,\mu = 59.8$ MPa with a standard deviation of 0.26 $\bar{\tau}_{\text{nuc}}$, $t_{\text{nuc}} = 2.6\times10^{6}\ B/\mu$ so that $L_{\text{nuc}} \approx 100b$ from equation (2); the annihilation distance $L_e = 6b$; the spacing between active slip planes $d = 100b$, see Fig. 4. The calculations are carried out at a strain rate six orders of magnitude greater than in the experiments in order to reduce the time required for the computations. However, as will be discussed subsequently, reducing the strain rate by two orders of magnitude does not change the behavior qualitatively.

The dimensions of the reference unit cell in Fig. 4 are specified by $L = 10$ μm so that the cell width is 20 μm and the cell height is 10 μm. Unless otherwise

stated, the area fraction of the wall material is $f = 0.4$. The density of dislocation sources in the matrix is $\rho^{m}_{nuc} = 1000L^{-2}$ (densities are normalized by a reference area $L\times L \equiv 10\times 10\ \mu m^2$ and superscripts m and w refer to matrix and wall material quantities, respectively) and the material is initially dislocation free.

Calculations are carried out for two cases: (i) dislocation nucleation in the wall material with $\rho^{w}_{nuc} = \rho^{m}_{nuc}$ and (ii) no dislocation nucleation in the wall material, $\rho^{w}_{nuc} = 0$. In both cases, the obstacles in the matrix material have strength $\tau^{m}_{obs} = 11.4\times 10^{-3}\mu = 296$ MPa and density $\rho^{m}_{obs} \approx 333L^{-2}$. For the wall material, the obstacle strength is $\tau^{w}_{obs} = 5\tau^{m}_{obs}$ and the obstacle density is $\rho^{w}_{obs} = 6\rho^{m}_{obs}$.

These parameter values were chosen to give effective yield strengths that are similar to the experimental values inferred from the hardness tests (see Section 2). The order of magnitude of the parameter values was estimated from the classical picture [15, 16] of the interactions between dislocations and obstacles, with the dislocations unpinning from obstacles over a distance of the order of the obstacle spacing. However, it is worth noting that the main interest here is the hardening at very small plastic strains, while the hardness measurements reflect a value of the strength after some plastic flow.

Figure 5(a) shows the resulting shear stress–strain response for each phase separately, while Fig. 5(b) gives the evolution of the total and mobile dislocation densities. A common feature is the absence of strain hardening. As in Refs 11 and 18, the overall response exhibits a yield stress corresponding to the generation of a sufficient number of mobile dislocations, followed by a plateau which is associated with the localization of dislocation activity on specific slip plane. The same trends were found for values between 0.2 $\bar{\tau}_{nuc}$ and 0.5 $\bar{\tau}_{nuc}$. The effective flow strength of the matrix material is about 25% lower than that of the wall material which is consistent with the hardness measurements of about a 20% difference, although the measurements have considerable scatter.

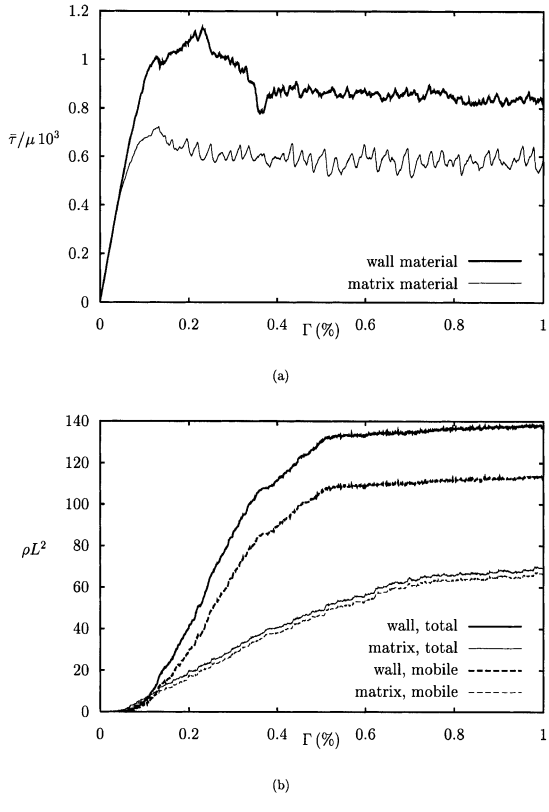

Fig. 5. Effect of obstacle parameters on the macroscopic phase properties: (a) overall shear stress response; (b) evolution of dislocation density. Matrix material: $\tau^{m}_{obs} = 11.4\times 10^{-3}\mu = 296$ MPa, $\rho^{m}_{obs} \approx 333L^{-2}$; wall material: $\tau^{w}_{obs} = 5\tau^{m}_{obs}$, $\rho^{w}_{obs} = 6\rho^{m}_{obs}$.

The wall material contains more and stronger obstacles than the matrix material so that the percentage of pinned dislocations is significantly higher in the wall material, Fig. 5(b). Dislocation pinning tends to increase the stress level which leads to an increase in nucleation activity on other slip planes. As a consequence, the total dislocation density is higher in the wall material and localization of slip is delayed.

4.1. Size effects

Size effects are investigated by considering cell size of $L/2$, L, $2\times L$ and $4\times L$, with the wall thickness scaled so that the area fraction of wall material is fixed. The density of dislocation sources and obstacles also remains fixed when varying size. The labels $L/2$, L, $2\times L$ and $4\times L$ are used to denote the four sizes analyzed. It is worth noting that the length scale $L = 10\ \mu m$ corresponds to the size of the fine dendrite microstructure and the length scale $4\times L$ corresponds to the size of the coarse dendrite microstructure in the experiments. In the calculations, the velocity at the cell boundaries is kept fixed, not the strain rate, so that the imposed strain rate is inversely proportional to the cell size. However, the rate dependence of the flow strength is slight so that the factor of eight change in strain rate over the full range of cell sizes considered gives rise to a only small decrease in flow strength with decreasing strain rate, which in any case is opposite to the direction of the size effect seen here.

Figure 6(a) shows the shear stress–strain response for the four length scales, with the wall material taken to be source free, $\rho^{w}_{nuc} = 0$. The hardening rate and the flow strength are higher for the $4\times L$ microstructure than for the microstructure with the reference size L, which is consistent with the experimental results. Generally, the overall hardening rate after an initial transient, say for $\Gamma \geq 0.2\%$, increases with increasing size although for sizes greater than $2\times L$ the hardening saturates. The reduction of the serrations in the stress–strain response with increasing size is directly related to the fact that we are carrying out a unit cell analysis: each event, such as the generation of new dipoles, occurs in every cell simultaneously; per unit volume, more events happen simultaneously in the smaller microstructures than in the larger ones.

Similar curves are shown in Fig. 6(b) with the den-

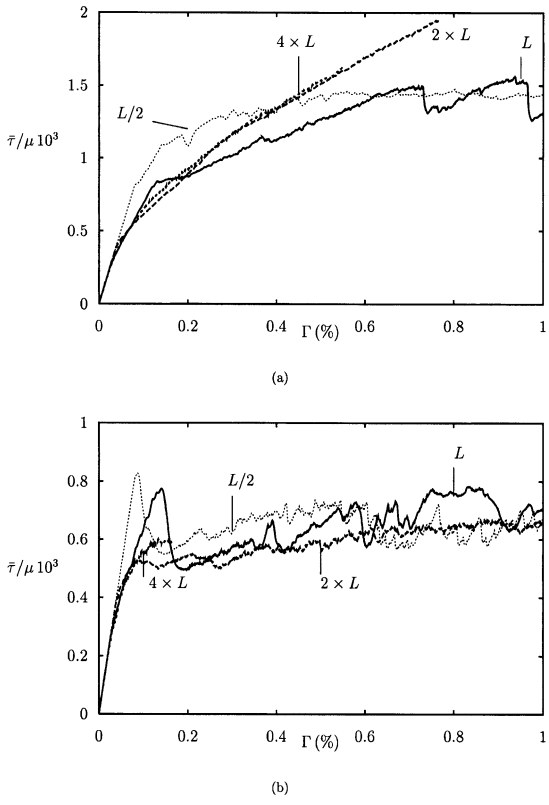

Fig. 6. The effect of size on the overall shear stress response: (a) source-free wall; (b) nucleation in wall. The reference case is labeled "*L*". Material parameters are: $L = 10$ μm, $W = 0.4L$, $\rho^{m}_{nuc} = 1000L^{-2}$, $\rho^{w}_{obs} = 2000L^{-2}$, $\rho^{m}_{obs} = \rho^{w}_{obs}/6$, $\tau^{w}_{obs} = 5.7\times10^{-2}\mu = 1.48$ GPa, $\tau^{m}_{obs} = \tau^{w}_{obs}/5$.

sity of sources in the wall and matrix being equal, $\rho^{m}_{nuc} = \rho^{w}_{nuc} = 1000L^{-2}$. In this case, the effect of size on the overall response is quite small, except for the initial stress peaks found for the smaller sizes *L* and *L*/2, which disappear for the larger cells. Nevertheless, the flow strength is insensitive to variations in cell size. Furthermore, with nucleation in the wall there is very little overall strain hardening.

Figure 7 shows the evolution of the total and mobile dislocation densities for the calculations with a source-free wall shown in Fig. 6(a). The dislocation density decreases with increasing size. Thus, the harder the response the lower the density of dislocations, averaged over the whole cell. For further insight, dislocation distributions for the four size scales are shown at the same strain level of $\Gamma = 0.4\%$ in Fig. 8. The cells are scaled with respect to their actual sizes. For the reference size scale *L*, Fig. 8(b), the first dislocations nucleate on the weakest slip planes but do not penetrate the wall. As a consequence, the number of pile-ups increases at the interface between the matrix and the wall. After sufficient overall shearing, some dislocations penetrate the wall. The two major stress drops in the overall response at about $\Gamma = 0.75\%$ and $\Gamma = 0.95\%$, Fig. 6(a), are associated with dislocations crossing the wall region.

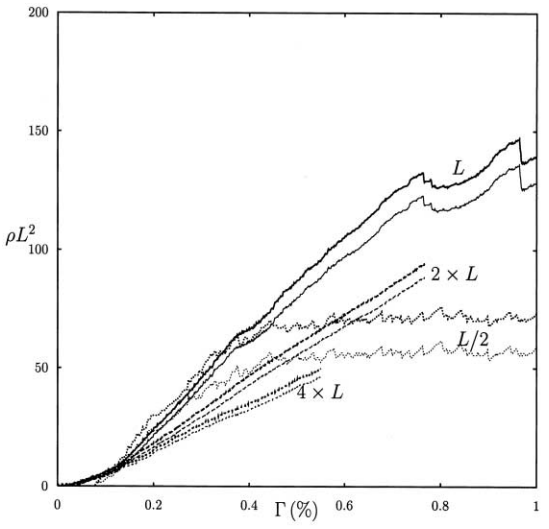

Fig. 7. The effect of size on the evolution of the dislocation density with a source-free wall. Thin lines are for mobile dislocations. The reference case is labeled "*L*".

For the finest microstructure, the *L*/2 case, the dislocations at $\Gamma = 0.4\%$ are almost exclusively concentrated in the wall, Fig. 8(a), although no dislocations nucleate in the wall. The formation of pile-ups at the wall–matrix interface for the 2×*L* and 4×*L* microstructures is seen in Figs 8(c) and (d). Especially for the largest size, the wall remains essentially elastic since dislocation motion is confined to a relatively thin boundary layer on either side of the wall. The elastic wall material must rotate to accommodate the shear and geometrically necessary dislocations at the wall–matrix interface give rise to the appropriate tilt boundaries. For a row of plate-like particles subjected to shear, the density of geometrically necessary dislocations, ρ^{G}, is estimated as [4]

$$\rho^{G} = \left(\frac{1}{\lambda^{G}}\right)\frac{2\Gamma}{b} \tag{4}$$

with λ^{G} equal to the inter-particle spacing. The dislocation density in the three largest microstructures decreasing with increasing size in Fig. 7 is consistent with equation (4), since the inter-particle spacing scales with *L*.

Another important characteristic of the dislocation distribution at the matrix–wall interface is the dislocation "penetration depth", defined as the maximum depth that a pile-up of dislocations extends into the wall material. At $\Gamma = 0.4\%$, as in Fig. 8, the penetration depth is about 0.8*W* and 0.6*W* for the *L*/2 and *L* microstructures, respectively. The average penetration depths are approximately *W*/4 for the 2×*L* microstructure and *W*/8 for the 4×*L* microstructure. For these two coarsest microstructures, the penetration depth is about 4 μm independent of the wall thickness. As shearing continues, the boundary layer

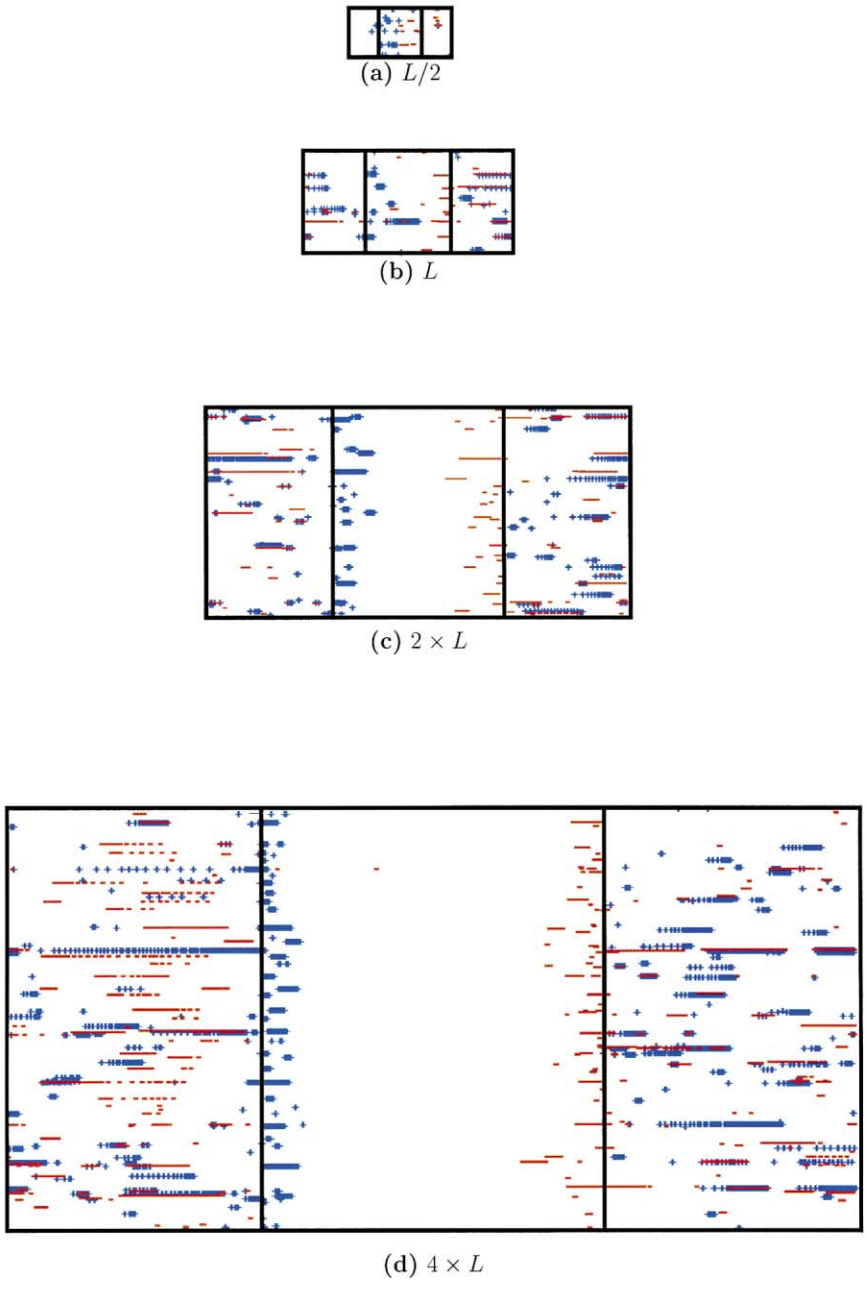

Fig. 8. Dislocation distributions in the four materials analyzed with a source-free wall, at $\Gamma = 0.4\%$. For the sake of clarity, the distributions of sources and obstacles are not shown.

does not penetrate further into the wall, at least for the range of strains considered here, but an increasing number of dislocations enter into existing pile-ups and new pile-ups form within the boundary layer. The penetration depth depends on the number of dislocations in the pile-ups at the matrix–wall interface and on the density and strength of the wall obstacles.

It is the development of geometrically necessary dislocations and the penetration of the wall that governs the hardening of the material. Geometrically necessary dislocations generally tend to lead to smaller being harder, as is indeed what has been observed by Cleveringa *et al.* [19] for similar discrete dislocation simulations of a composite material. Here, however, the development of pile-ups of geometrically necessary dislocations competes with the partial or complete penetration of the wall. When dislocations penetrate the wall, the hardening is low, see Fig. 6(a). On the other hand, for the $2\times L$ and $4\times L$ microstructures there are two counterbalancing effects that essentially cancel. The geometrically necessary dislocations associated with the pile-ups at the matrix–wall interface tend to induce higher hardening in the smaller microstructure, while the rela-

tively greater slip penetration into the wall for the smaller microstructure tends to make the smaller microstructure softer.

Figure 9 shows plots of the slip in the $L/2$, L and $2\times L$ microstructures with the convention that the slip is zero at the middle of the cell. This convention involves no loss in generality because the net Burgers vector is zero in the cell due to periodicity and only dipoles are generated. The overall shear strain is $\Gamma = 0.6\%$, which is somewhat higher than the strain level in Fig. 8. The slip is computed in units of the Burgers vector b. For the $L/2$ and L microstructures, slip bands penetrate rather far into the wall. On the other hand, the penetration depth of the slip bands in the $2\times L$ and $4\times L$ microstructures is confined to the pile-ups of geometrically necessary dislocations at the matrix–wall interface. This picture is consistent with the experimental observations in Fig. 3.

Although stress contours are not shown here, large stress concentrations do develop at the wall–matrix interface. To quantify the stress concentration, Table 1 gives average shear stresses in the phases, as defined by

$$\langle \sigma_{12} \rangle_{\mathrm{p}} = \frac{1}{V_{\mathrm{p}}} \int_{V_{\mathrm{p}}} \sigma_{12} \, \mathrm{d}V \tag{5}$$

where $p = \mathrm{c,m,w}$ for averaging over the cell, the matrix and the wall, respectively. The macroscopic shear stress $\bar{\tau}$ is the same as the cell average $\langle \sigma_{12} \rangle_{\mathrm{c}}$, and is related to the phase averages by

$$\bar{\tau} = (1-f)\langle \sigma_{12} \rangle_{\mathrm{m}} + f\langle \rho_{12} \rangle_{\mathrm{w}}. \tag{6}$$

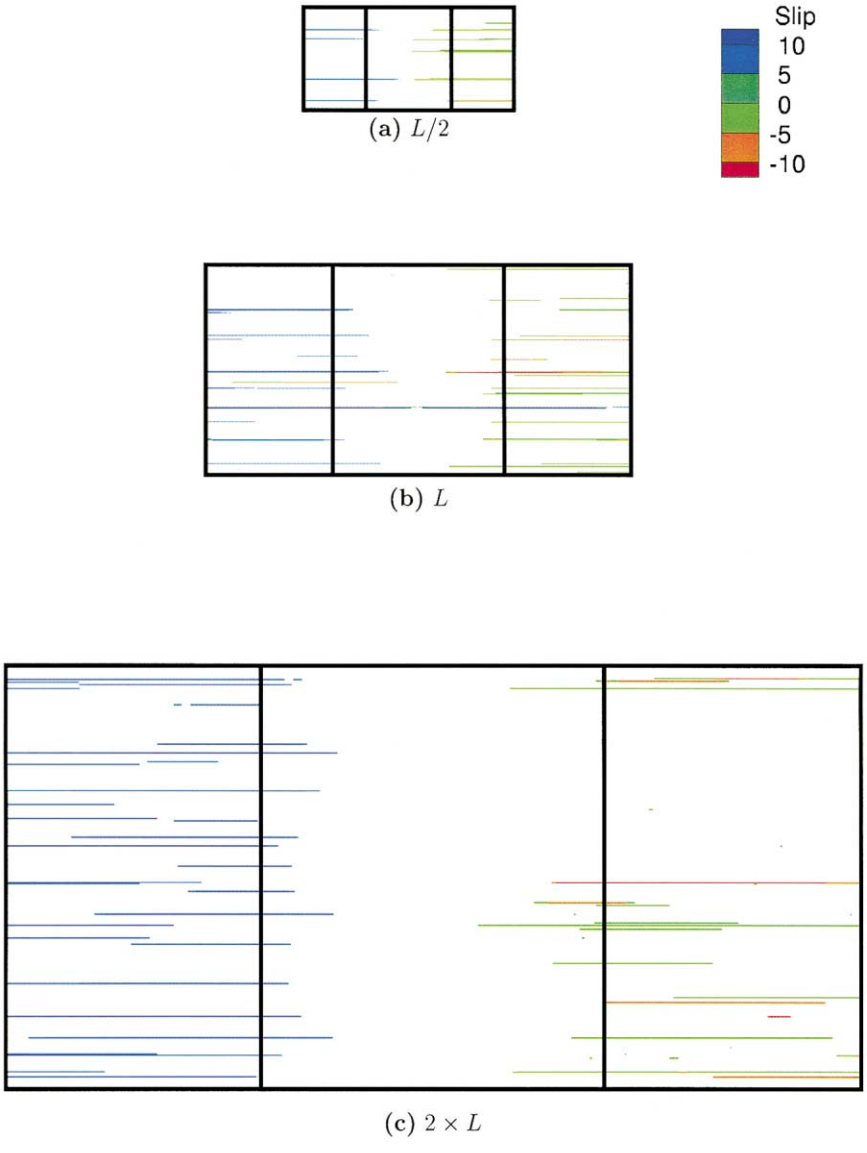

Fig. 9. Slip plots in three of the four materials analyzed with a source-free wall, at $\Gamma = 0.6\%$.

Table 1. Phase average shear stresses for the four sizes analyzed. The reference material which corresponds to the fine microstructure is labeled "*L*". Material parameters are: $L = 10$ μm, $W = 0.4L$, $\rho^{m}_{nuc} = 1000L^{-2}$, $\rho^{w}_{obs} = 2000L^{-2}$, $\rho^{m}_{obs} = \rho^{w}_{obs}/6$, $\tau^{w}_{obs} = 5.7\times10^{-2}\mu = 1.48$ GPa, $\tau^{m}_{obs} = \tau^{w}_{obs}/5$

Material	Γ	$<\sigma_{12}>/\mu\times10^{3}$			$<\sigma_{12}>/\bar{\tau}$	
	(%)	Cell	Matrix	Wall	Matrix	Wall
L/2	0.30	1.31	1.00	1.83	0.76	1.39
L/2	0.60	1.43	0.92	2.23	0.64	1.37
L/2	0.90	1.39	0.89	2.19	0.64	1.57
L/2	1.20	1.43	0.90	2.25	0.63	1.58
L/2	4.0	1.44	0.89	2.31	0.62	1.60
L	0.25	0.94	0.62	1.41	0.62	1.51
L	0.32	1.03	0.60	1.69	0.58	1.64
L	0.50	1.25	0.59	2.23	0.48	1.79
L	0.60	1.38	0.57	2.59	0.42	1.88
L	1.0	1.29	0.38	2.66	0.29	2.06
2×*L*	0.44	1.35	0.48	2.66	0.48	1.97
2×*L*	0.60	1.66	0.43	3.53	0.26	2.57
2×*L*	0.70	1.82	0.41	3.93	0.23	2.16
2×*L*	0.77	1.92	0.39	4.22	0.20	2.19
4×*L*	0.35	1.25	0.42	2.50	0.34	2.00
4×*L*	0.55	1.61	0.38	3.44	0.24	2.14

At any level of deformation and for all cases considered, the average stress level is higher in the wall than in the matrix. Higher stresses in the wall, of course, tend to promote fracture in the Si particles, which is consistent with the experimental observation of Si particle fracture in the boundary eutectic region. At the same macroscopic shear strain $\Gamma = 0.6\%$, the average shear stress in the matrix, $\langle\sigma_{12}\rangle_m$, relative to the macroscopic shear stress, $\bar{\tau}$, decreases with increasing size from about 0.64 for the *L*/2 microstructure to 0.25 for the 4×*L* microstructure. The absolute value of $\langle\sigma_{12}\rangle_m$ is halved for the same increasing size range. On the other hand, the normalized average shear stress in the wall $\langle\sigma_{12}\rangle_w/\bar{\tau}$ is almost doubled. In the two coarsest microstructures, local averaging over columns in the wall, close to the wall–matrix interface, indicates that the stress concentration at the interface is further enhanced compared to the two finest microstructures. The stress elevation in the wall material is associated with the geometrically necessary dislocations at the wall–matrix interface.

Phase-average shear stresses were computed for the *L*/2, *L* and 2×*L* microstructures at various stages of deformation. When significant hardening is obtained, such as with the 2×*L* microstructure, the average stress in the wall, $\langle\sigma_{12}\rangle_w$, significantly increases while the average stress in the matrix remains roughly constant around $0.45\times10^{-3}\mu$. By way of contrast, for the *L*/2 microstructure, the average stress is independent of plastic strain in both wall and matrix with $\langle\sigma_{12}\rangle_w \approx 2.20\times10^{-3}\mu$ and $\langle\sigma_{12}\rangle_m \approx 0.90\times10^{-3}\mu$, respectively. This is consistent with the observation in Fig. 7 that a steady-state dislocation density is attained, leading to almost no hardening after $\Gamma \approx 0.4\%$. The situation in the reference *L* microstructure is an intermediate case.

A calculation was carried out for the *L*/2 microstructure with the strain rate reduced by two orders of magnitude. The response was not qualitatively changed relative to that in Fig. 6(a). The initial yield behavior was essentially the same in the low rate and high rate calculations, but the stress level of the plateau in the stress–strain curve was reduced by about 8%. Further evidence that the calculations give behavior representative of that seen in the experiments was obtained from a stress relaxation calculation for the *L* microstructure. After some initial plasticity (the stress increased about 50% above its value at initial yield), the applied shear strain was held constant and the overall shear stress quickly dropped by less than 1% and then stayed essentially constant.

4.2. Parameter studies

4.2.1. Density of wall sources. The results in Fig. 6 show that the overall strain hardening is quite sensitive to whether or not nucleation occurs within the wall. An intermediate density of wall sources of $\rho^{w}_{nuc} = 500L^{-2}$ is analyzed for the microstructure with the reference size *L*. Figure 10 summarizes the influence of the density of wall sources on the overall response when the standard deviation of the nucleation strengths is $0.26\ \bar{\tau}_{nuc}$. At small strains, halving the density of wall sources gives a stress level which is intermediate between the case with density $\rho^{w}_{nuc} = 1000L^{-2}$ and the case with a source-free wall, $\rho^{w}_{nuc} = 0$. At larger strains, there is little difference in stress level between the calculations with $\rho^{w}_{nuc} = 1000L^{-2}$ and $\rho^{w}_{nuc} = 500L^{-2}$. The source distri-

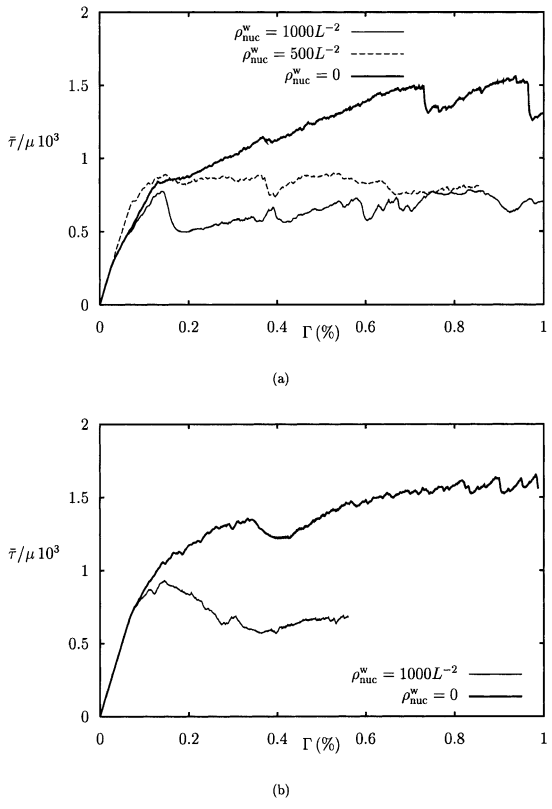

Fig. 10. Effect of the density of wall sources on the overall shear stress response for the reference size L, using a mean nucleation strength $\bar{\tau}_s = 2.3\times10^{-3}\mu$ with a standard deviation of (a) 0.26 $\bar{\tau}_{nuc}$ and (b) 0.23 $\bar{\tau}_{nuc}$. The reference value is $\rho^{w}_{nuc} = 1000L^{-2}$.

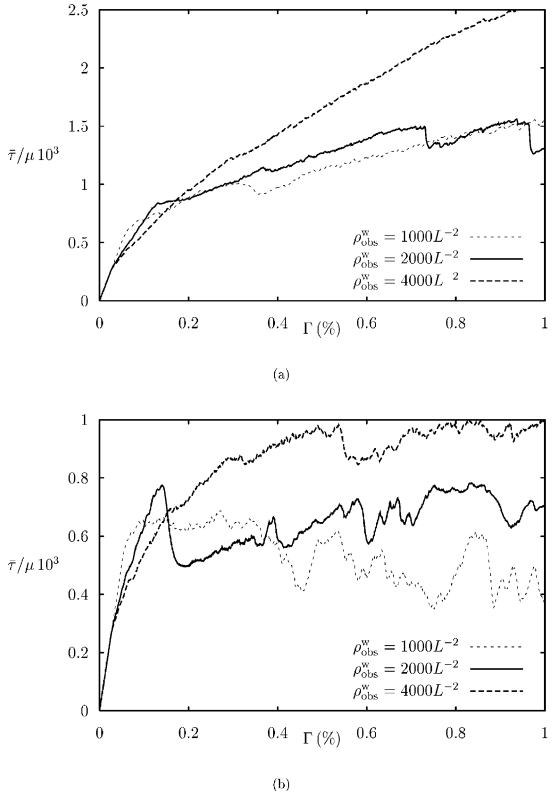

Fig. 11. Effect of the density of wall obstacles on the overall shear stress response for the reference size "L": (a) source-free wall; (b) nucleation in wall. In both cases, the reference density is $\rho^{w}_{obs} = 2000L^{-2}$.

butions for the cases with $\rho^{w}_{nuc} = 1000L^{-2}$ and $\rho^{w}_{nuc} = 500L^{-2}$ were generated independently so that there is also a statistical effect.

4.2.2. Density of wall obstacles. The extent to which the density of wall obstacles controls the penetration depth is addressed by varying this density from one half to twice the reference value $\rho^{w}_{obs} = 2000L^{-2}$. Recall that the density of matrix obstacles is much lower $\rho^{m}_{obs} = 333L^{-2}$. The calculations are carried out for the microstructure characterized by the reference length L, and cases with and without nucleation in the wall are considered. The results for a source-free wall are shown in Fig. 11(a). For the highest density of wall obstacles there is a considerable amount of strain hardening and the stress level after 1% of deformation is about five times its value at yield. On the other hand, the macroscopic stress–strain response obtained with $\rho^{w}_{obs} = 1000L^{-2}$ differs little from the one obtained for the reference case using $\rho^{w}_{obs} = 2000L^{-2}$.

A closer examination of dislocation distributions for the three cases analyzed shows that with $\rho^{w}_{obs} = 4000L^{-2}$, pile-ups form at the wall–matrix interfaces in a similar manner as in Figs 8(c) and (d). The penetration depth is estimated at about 2 μm (i.e. $W/4$). This value does not evolve with increasing deformation; only the number of pile-ups along the interface increases. The boundary layer obtained with $\rho^{w}_{obs} = 4000L^{-2}$ is about half the thickness of the one obtained with $\rho^{w}_{obs} = 2000L^{-2}$, illustrating that the boundary layer thickness increases with decreasing obstacle density. There is an upper limit to the boundary layer thickness, which is half the wall thickness, $W/2$. As the boundary layer thickness approaches this value, the wall no longer effectively blocks slip. This is shown for the case with $\rho^{w}_{obs} = 2000L^{-2}$, by the dislocation distribution, Fig. 8(b), and by the corresponding slip plot, Fig. 9(b). Similar pictures are obtained for the calculations with wall obstacle density $\rho^{w}_{obs} = 1000L^{-2}$. For both $\rho^{w}_{obs} = 2000L^{-2}$ and $\rho^{w}_{obs} = 1000L^{-2}$, dislocation mobility within the wall is high enough to lead to a lower limit for the hardening rate as shown in the response in Fig. 11(a).

When a boundary layer forms, the hardening rate is essentially controlled by the density of geometrically necessary dislocations at the matrix–wall interface, which depends on ρ^{w}_{obs}. When a boundary layer does not form, the overall hardening rate is essentially independent of the density of wall obstacles, as seen by comparing the cases with $\rho^{w}_{obs} = 2000L^{-2}$ and $\rho^{w}_{obs} = 1000L^{-2}$ in Fig. 11(a), at least over the range of densities considered.

Figure 11(b) illustrates the effect of varying the

density of wall obstacles when nucleation in the wall takes place. The nucleation of dislocations inside the wall prevents boundary layers from being formed. Subsequently, the stresses do not build up as in the case with no nucleation in the wall, and the rate of strain hardening is then about a factor of three smaller. Even though a boundary layer does not form, there is an effect of ρ^{w}_{obs} on the overall stress–strain response. As a consequence of increasing the density of wall obstacles, the density of dislocations pinned inside the wall significantly increases. When the obstacle density is $\rho^{w}_{obs} = 1000L^{-2}$, dislocation activity localizes on a few slip planes after less than 0.2% of macroscopic shear strain, with the dislocations having crossed the wall from both sides.

4.2.3. Wall thickness. The results presented so far have illustrated the effect of boundary layers on the average hardening modulus. We now investigate the effect of wall thickness on the overall response in circumstances in which a boundary layer is not formed. Hence, in this section the area fraction of wall material, f, varies. The effect of wall thickness on the overall stress–strain response and on the evolution of the dislocation density is shown in Fig. 12 for the reference microstructure size L using the reference density of wall obstacles $\rho^{w}_{obs} = 2000L^{-2}$ and with no dislocation nucleation in the wall. A boundary layer does not form for either case in Fig. 12. The stress–strain response obtained with a wall thickness of $W/2$ differs from that with a wall thickness of W in two respects. First, the yield point is lower and secondly the hardening rate is lower.

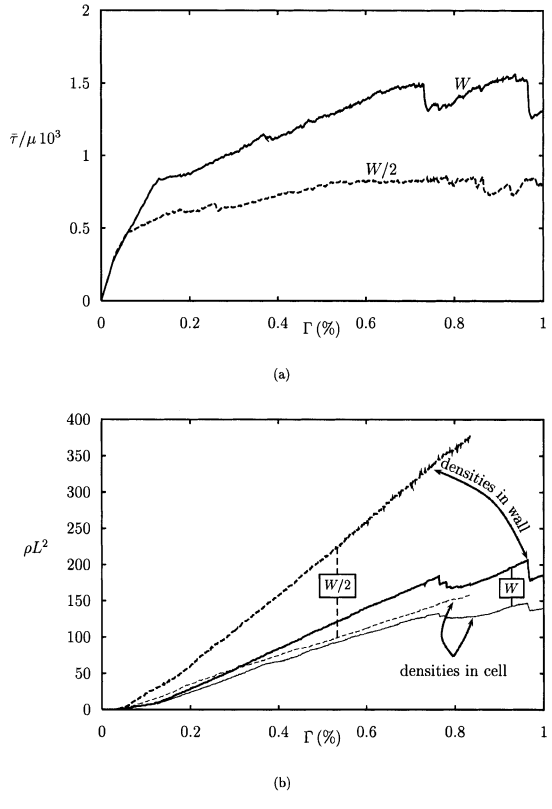

Fig. 12. The effect of wall thickness for a material with a source-free wall: (a) overall shear stress response; (b) evolution of dislocation density. The reference case is labeled "W" ($\equiv 0.4L$).

Figure 12(b) shows that the dislocation densities for these two cases are essentially the same throughout the deformation history (thin lines in the figure). However, these densities are calculated considering the entire cell. If one calculates the dislocation densities in the wall alone then the results differ significantly, as seen from the corresponding curves in Fig. 12(b). The tendency for dislocation activity to occur within the wall is enhanced for a thinner wall. In addition, whatever the wall thickness, the dislocation density in the wall is higher than in the entire cell. For instance, Fig. 12(b) shows that at $\Gamma = 0.8\%$ the density in the wall is more than twice the density in the cell for the case with $W/2$ whereas it is just 30% higher for the case with wall thickness W.

In both cases, most of the dislocations in the wall are mobile; the dislocations that are pinned represent less than 10% of the total density in the wall material. It is then inferred from Fig. 12(b) that the dislocation mobility inside the wall is higher for the thinner wall, which is consistent with the lower hardening in this case, Fig. 12(a).

Shear stress averages are compared in Table 2 at two strain levels. In spite of the two abrupt drops of the stress level for the case with a wall thickness of W, at $\Gamma \approx 0.75\%$ and $\Gamma \approx 0.95\%$, Fig. 12(a), the increase of the average stress in the wall is greater than for the case with a wall thickness of $W/2$. Thus, the increased hardness for the case with wall thickness W can be seen in two effects in equation (6): (i) the volume fraction f of the harder wall material is increased and (ii) due to the lower density of mobile dislocations, the average shear stress in the wall, $\langle \sigma_{12} \rangle_w$, is increased.

5. CONCLUSIONS

- Tensile tests carried out on specimens of cast aluminum alloy A356-T6 exhibit an inverse size effect—specimens with a finer microstructure have lower flow strength than specimens with a coarser microstructure.
- The thickness of the boundary eutectic region of segregated silicon particles scales with the size of the secondary dendrite arm spacing.
- Discrete dislocation analyses of a model two-phase material were carried out where the wall phase differs from the matrix phase in having a different density and strength of point obstacles.
- Two cases were considered: (i) the same density of dislocation sources in the wall and in the matrix and (ii) no dislocation sources in the wall, which is consistent with the AFM-based observations in Fig. 3(c).
- The inverse size effect emerges when dislocation

Table 2. Phase average shear stresses for the reference size "*L*" using two different values of the boundary thickness. The reference material which corresponds to the fine microstructure is labeled "*W*"

Material	Γ	$<\sigma_{12}>/\mu\times10^3$			$<\sigma_{12}>/\bar{\tau}$	
	(%)	Cell	Matrix	Wall	Matrix	Wall
W/2	0.25	0.65	0.54	1.12	0.83	1.71
W/2	1.0	0.80	0.55	1.83	0.68	2.28
W	0.25	0.94	0.62	1.41	0.62	1.51
W	1.0	1.29	0.38	2.66	0.29	2.06

nucleation is precluded in the wall. For a sufficiently small-scale microstructure, the wall does not inhibit dislocation glide and a size independent response is obtained. For a sufficiently large-scale microstructure, dislocation glide is limited to a boundary layer of geometrically necessary dislocations near the wall–matrix interface, and the response is also relatively size independent, albeit considerably harder than the small-scale microstructure. For intermediate size microstructures, the strength increases with the size because thicker walls are more effective at blocking slip.

- When dislocation nucleation takes place within the wall, no size effect is obtained if the density of sources in the wall is sufficiently high. For the inverse size effect to be obtained, slip must be effectively precluded in the wall material.
- Although the single slip discrete dislocation model is too simplified to provide a quantitative description of the experimental observations, the mechanism for the inverse size effect is clearly revealed. At small strains, glide is effectively blocked by the boundary eutectic region of segregated silicon particles for the coarser microstructure giving an increased initial hardening rate. At larger strains, the high stresses in the boundary eutectic region are eventually relaxed by dislocation nucleation or by fracture of the Si particles.
- The experiments and the discrete dislocation model together clearly illustrate a mechanism that can provide an inverse size effect in a broader range of circumstances than specifically considered here.

Acknowledgements—We are pleased to acknowledge support from the Materials Research Science and Engineering Center on *On Micro-and-Nano-Mechanics of Electronic and Structural Materials* at Brown University (NSF Grant DMR-0079964). Support from the Caterpillar Corporation and from the Ford Motor Company is also gratefully acknowledged.

REFERENCES

1. Hall, E. O., *Proc. Phys. Soc. London*, 1951, **B64**, 747.
2. Petch, N. J., *J. Iron Steel Inst. London*, 1953, **174**, 25.
3. Nye, J. F., *Acta metall.*, 1953, **1**, 153.
4. Ashby, M. F., *Phil. Mag.*, 1970, **21**, 399.
5. De Guzman, M. S., Neubauer, G., Flinn, P. and Nix, W. D., *Mater. Res. Symp. Proc.*, 1993, **308**, 613.
6. Fleck, N. A., Muller, G. M., Ashby, M. F. and Hutchinson, J. W., *Acta metall. mater.*, 1995, **42**, 475.
7. Ma, Q. and Clarke, D. R., *J. Mater. Res.*, 1995, **10**, 853.
8. Stölken, J. S. and Evans, A. G., *Acta mater.*, 1998, **46**, 5109.
9. Chokshi, A. H., Rosen, A., Karch, J. and Gleiter, H., *Scripta metall.*, 1989, **23**, 1679.
10. Arzt, E., *Acta mater.*, 1998, **46**, 5611.
11. Cleveringa, H. H. M., Van der Griessen, E. and Needleman, A., *Acta mater.*, 1997, **45**, 3163.
12. Boileau, J. M., Zindel, J. W. and Allison, J. E., in *Applications for Aluminum in Vehicle Design*. SAE International, Warrendale, PA, 1997, p. 61.
13. McLellan, D. L., *J. Testing Evaluation*, 1980, **8**, 170.
14. Kubin, L. P., Canova, G., Condat, M., Devincre, B., Pontikis, V. and Bréchet, Y., in *Nonlinear Phenomena in Materials Science*, ed. J. Martin and L. P. Kubin. Sci-Tech, Vaduz, 1992, p. 455.
15. Nabarro, F. R. N., *Theory of Crystal Dislocations*. Oxford University Press, 1967.
16. Hirth, J. P. and Lothe, J., *Theory of Dislocations*. McGraw-Hill, New York, 1968.
17. Lubarda, V., Blume, J. A. and Needleman, A., *Acta metall. mater.*, 1993, **41**, 625.
18. Van der Giessen, E. and Needleman, A., *Modelling Simul. Mater. Sci. Eng.*, 1995, **3**, 689.
19. Cleveringa, H. H. M., Van der Giessen, E. and Needleman, A., *J. Phys. IV*, 1998, **8 P4**, 83.